Chapter 2

A Current-Driven Resonant Dual Active Bridge Converter with Dual Source Property for Optimal Battery Charging

2.1 Introduction

An optimal battery charging strategy is the one that can charge the battery at faster rates while ensuring maximum battery life. As discussed in the literature in Chapter 1, there exist several optimal battery charging strategies out of which the constant current-constant voltage (CC-CV) charging strategy is the most popular and well-adapted charging technique due to its ability to ensure efficient power transfer and battery protection. In this strategy, when the battery state-of-charge is low, the entire charging circuit behaves as a current source and applies a constant charging current to the battery. Whereas, when the battery voltage builds up to reach its near-optimal value, the charging circuit transitions smoothly to behave as a voltage source, thus ensuring constant-voltage charging at the battery terminal. Hence, the CC-CV charging is mainly characterized by its current-source property, voltage-source property, and the smooth transition between them.

An optimal battery charger is expected to perform efficient charging in both CC and CV modes, offering a wide gain range as well as ensuring a robust converter. However, the converters reported in the existing literature required complex control circuits to achieve current-source property and voltage-source property, and to enable smooth transition from a single converter for CC-CV charging. In addition to the system complexity the existing methods also increased the computational cost, memory requirement, power loss, and overall response time of the system. Considering the challenges associated with using complex modulation techniques, variable frequency operation and higher order resonant tank circuits, fixed frequency resonant converters operating at load independent points to achieve CC-CV behavior are the best choice of converter for optimal battery chargers.

The desired features of an optimal EV battery charger are as listed below:

i) Bi-directionality to support features like vehicle-to-grid (V2G) and grid-to-vehicle (G2V) operation.
ii) High power density for compact size.
iii) Soft-switching operation for reduced losses
iv) Paralleling capability for fast charging
v) Galvanic isolation for safety

To meet the above requirements of an optimal battery charger, a novel current-driven bi-frequency resonant dual active bridge converter for efficiently charging a battery in CC-CV mode is presented in this chapter for EV charging applications. A representative block diagram of the proposed charger is shown in Fig. 2.1.

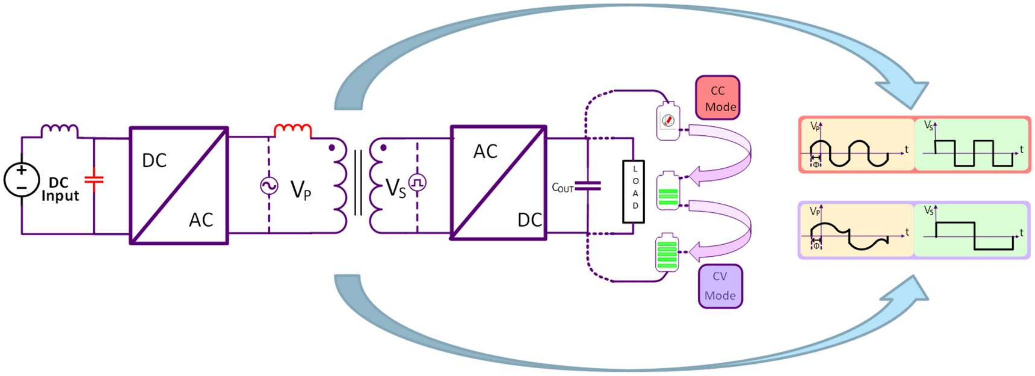

Fig. 2.1 Proposed Scheme of CC-CV Charging using single Current Fed Resonant Dual Active Bridge Converter

The novel converter gives the freedom to operate without complex control, while ensuring stable voltage and current regulation to achieve CC-CV charging. Due to the converter configuration, the switching states cause the converter to form an equivalent parallel resonant tank, which facilitates the proposed converter to behave as a current source and a voltage source using a single step change in frequency and thus, offering dual source property at its output. In addition, the problem of input current ripple is eliminated, improving converter reliability, size, and weight due to the replacement of electrolytic capacitors by a resonant film capacitor.

The details of the proposed EV charger, including its mathematical modelling and operation, are presented in this chapter. The behavior of the converter is analyzed through state-plane analysis, and the trajectory of each interval with the closed-form solution is presented. To verify the behavior of the proposed converter, a scaled-down 500 W experimental prototype is developed in the laboratory. The performance of the proposed charger is validated with varying resistance to emulate the behavior of the battery under charge. The results are presented for both CC and CV charging modes and the transition from CC to CV mode. A Texas Instruments TMS320F28335 DSP board is used for implementing the proposed control technique.

In the proposed topology, the electrolytic filter capacitor at the input side is replaced by a small film capacitor, which is used as a resonant capacitor for improving size, weight, and reliability.

2.2 The Proposed Optimal Battery Charger

In view of the above discussion, this chapter presents a current-driven bi-frequency resonant dual active bridge converter which is capable of acting as both a current source and a voltage source without requiring a dedicated controller. The proposed converter is reliable, efficient, and facilitates CC-CV charging with minimal control. In the proposed topology, the electrolytic filter capacitor at the input side is replaced by a small film capacitor, which is used as a resonant capacitor for improving size, weight, and reliability. The overall contribution of the proposed work is listed as follows.

- The proposed resonant converter operates at two different but fixed frequencies to behave as a current source and a voltage source for battery charging operation in CC-CV mode. This eliminates the need for a complex controller and results in reduced implementation cost.
- Fixed frequency operation of the converter makes the magnetics design simple with its optimum utilization.
- Resonant tank is formed between the input filter capacitor and the leakage inductance of the isolation transformer; thus, eliminating the need for an additional element to form the tank.
- All the inverter switches undergo zero voltage switching (ZVS) for CC mode. Further, for CV mode, the inverter switches achieve zero current switching

(ZCS), whereas the rectifier switches achieve ZVS. This soft-switching transition at high frequency proves to be a substantial cut at losses and results in much improved efficiency.

- As the input filter capacitor itself is made to resonate, the conventionally used electrolytic capacitor, which deteriorates over a comparatively shorter period of time, can be replaced by a metal film capacitor having a much longer life span. This improves the overall reliability of the converter.

The proposed converter for optimal battery charging is shown in Fig. 2.2. The source inductor L_{in} makes it a current-fed DAB whose input filter capacitor C_r resonates with the leakage inductance L_r of the isolation transformer to form a parallel resonant tank. Its application as an optimal battery charger is realizable due to the converter's features of parallel resonance obtained by the proposed configuration, i.e., behaving as a current source and a voltage source at resonant and half-resonant frequency, respectively.

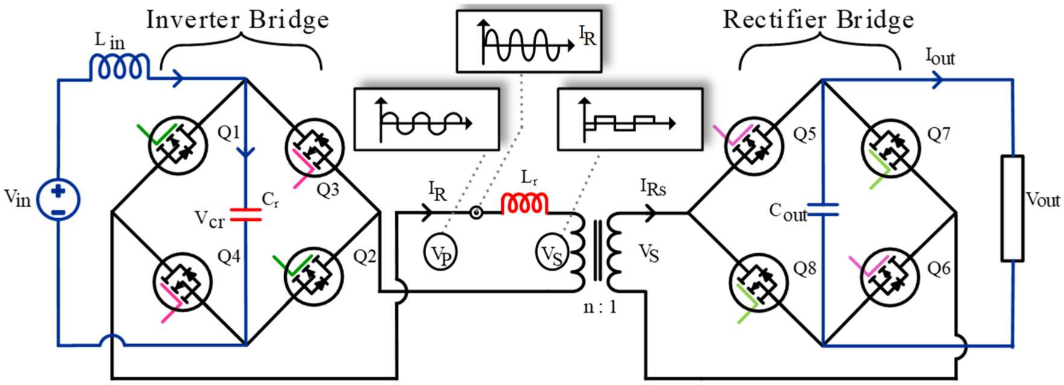

Fig. 2.2 Proposed current-driven bi-frequency resonant dual active bridge converter

A few assumptions are made to simplify the analysis of the converter. The input filter inductor L_{in} is large enough to maintain a constant current I_{in} at the input. The output voltage remains constant due to the presence of the filter capacitor C_{out}. The deadtime between switching instant and the effect of parasitic elements has been ignored during the modelling of the converter.

2.2.1 Circuit Configuration

The behavior of the proposed topology is governed by the switching pattern of the two active bridges, viz., the inverter bridge at the input and the rectifier bridge at the output.

The inverter bridge is fed from a DC source, Vin, connected in series with a filter inductor, L_{in}. The filter inductor eliminates the source current ripple. Further, the capacitor C_r of the resonant tank is placed before the switching network. This causes a resonant voltage v_{cr} to appear across the conducting switches of the inverter bridge. As a result, the switch voltage V_{DS} decays well before the application of the gate pulse. Thus, enabling soft-switching and eliminating the switching losses. The rectified output is filtered by a capacitor C_{out} that powers the battery or the DC load connected at the output.

2.2.2 Modulation Strategy

A diagram of switching strategy for optimal battery charging implementation is shown in Fig. 2.3 (a) and (b).

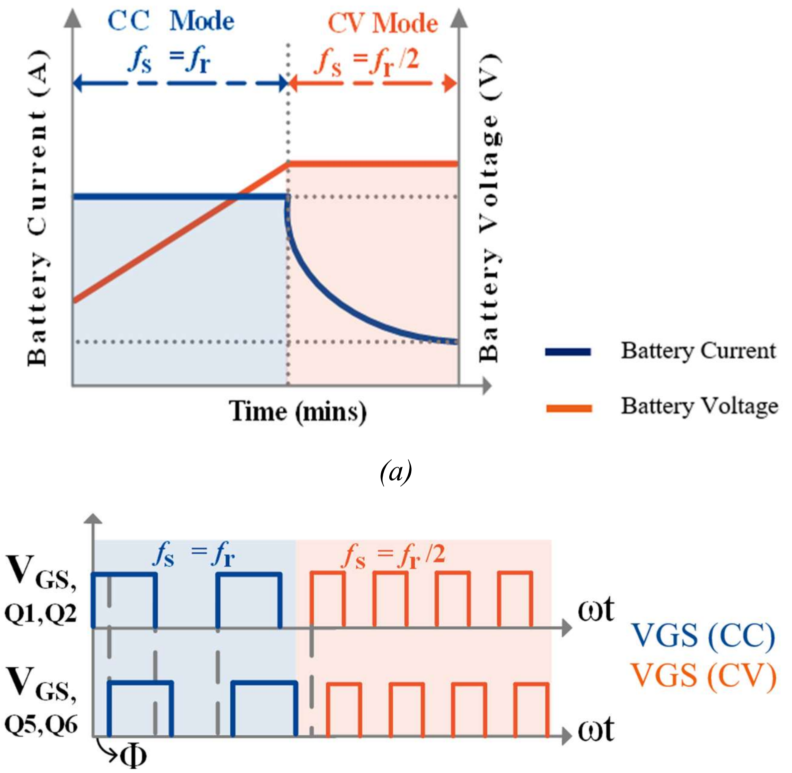

(a)

(b)

Fig. 2.3 Optimal charging scheme implementation using proposed converter (a) CC-CV Charging (b) Switching strategy.

The converter operates in CC mode when the switching frequency is equal to the resonant frequency, whereas it works in CV mode when the converter operates at half of the resonant frequency. V_{GS} for Q1, Q2 and Q5, Q6 are shown in Fig. 2.3 (b), switches Q3, Q4 and Q7, Q8 operate in complimentary manner. Each of the diagonal switch pair of both bridges operate for 50% duty with a small deadtime. Further, rectifier bridge switches operate at a phase shift (Φ) concerning the corresponding switches of the inverter bridge. The direction and the amount of power flow can be controlled by adjusting the phase shift (Φ), whereas mode change from CC to CV is achieved by a single step change in the switching frequency f_s. Thus, the converter works on a fixed frequency variable phase shift modulation technique. Consequently, the complexity of control and design challenges associated with variable frequency modulation of the resonant converter is eliminated.

2.2.3 Operation as Parallel Resonant Converter

Fig. 2.4 represents the equivalent circuit of the proposed converter. The equivalent circuits are referred to as their primary side with $V'_{out} = nV_{out}$ for ease of representation. An equivalent DC current source replaces the source inductor and DC voltage combination. The tank output voltage is a square wave with magnitude ± V'_{out}. From the equivalent circuit, it can be clearly inferred that the input filter capacitor and leakage inductance form a parallel resonant tank. The mathematical equations corresponding to the equivalent tank circuit may be derived as:

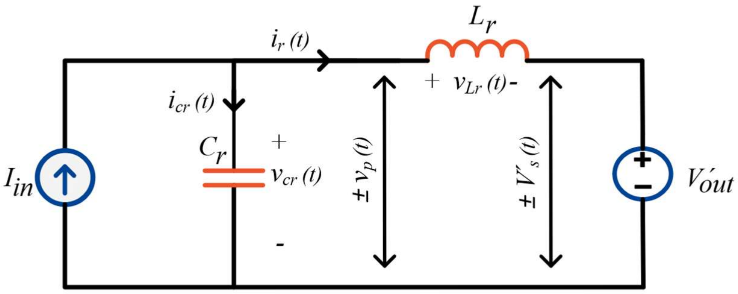

Fig. 2.4 Equivalent circuit of the proposed converter.

$$L_r \frac{di_r(t)}{dt} = v_p(t) - V'_s \tag{2.1}$$

$$C_r \frac{dv_{cr}(t)}{dt} = I_{in} - i_r(t) \tag{2.2}$$

Where v_p and V_s' are the transformer terminal voltages on inverter and rectifier side, respectively. The variables i_r and v_{cr} represents the resonant current and voltage. The characteristic impedance of the tank circuit is $Z_o = \sqrt{L_r/C_r}$ and resonant frequency of the tank is given by $\omega_o = 1/\sqrt{L_r C_r}$.

2.3 Operation Principle and State Plane Analysis of the Proposed Charger

The steady state analysis of the equivalent parallel resonant converter presents complicated algebraic equations. Recent works have explored state-plane analysis (SPA) for the analysis of complicated resonant converters [25]–[28]. For the state-plane analysis, the converter parameters are normalized with base quantities as indicated in Table 2.1. The inductor current i_r and capacitor voltage v_{cr} are selected as the state variables. Since the modulation strategy of the current and voltage regulation mode is exactly the same, except for the switching frequency, the converter operation in each of the switching intervals can be explained for CC mode, and it can be applied identically to CV mode. Typical waveforms of converter operation in each mode are shown in Fig. 2.5 (a) and (b). Complete converter operation is shown in Fig. 2.6 to Fig. 2.9.

Table 2.1 Base Values and Normalized Parameters of the Proposed Converter

Symbol	Parameter	Value
Base Quantities:		
Z_{base}	Base impedance	$\sqrt{L_r/C_r}$
V_{base}	Base voltage	nV_{out}
I_{base}	Base current	$nV_{out}/\sqrt{L_r/C_r}$
f_{base}	Base frequency	$1/2\pi\sqrt{L_rC_r}$
Normalized Quantities:		
M	Normalized Input voltage	V_{in}/V_{base}
J	Normalized Input current	I_{in}/I_{base}
m_{Cr}	Normalized Capacitor voltage	v_{cr}/V_{base}
j_{Lr}	Normalized inductor current	i_r/I_{base}
F	Normalized switching frequency	f_s/f_{base}

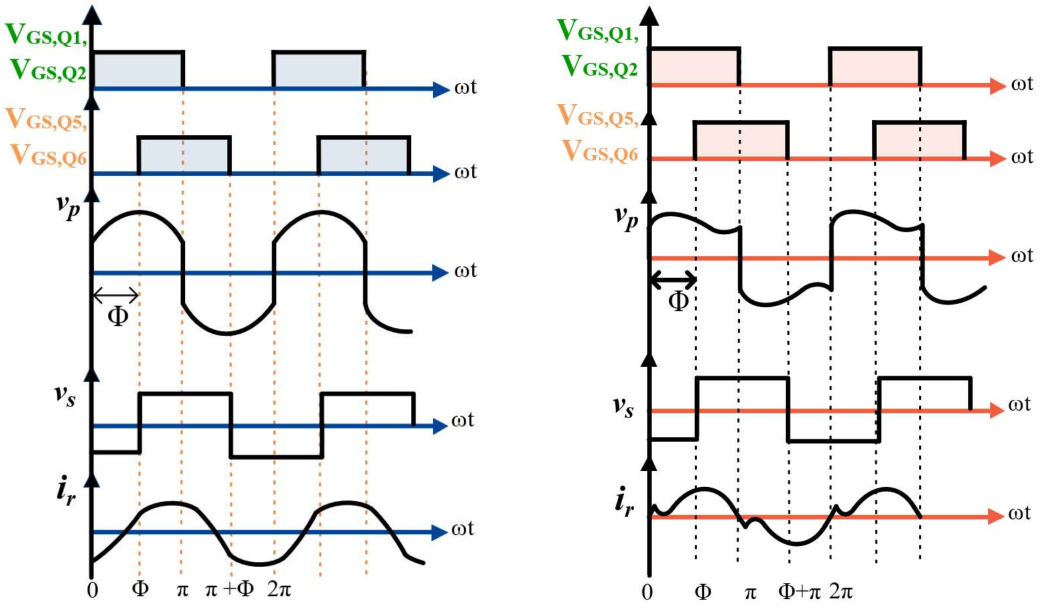

(a) *(b)*

Fig. 2.5 Current and voltage waveform of proposed converter in (a) CC mode (b) CV mode.

Under all resonance conditions, the converter switches between four intervals depending on the switching instant. This means the state-plane trajectory and hence, the closed-form solution comprises four partial trajectories representing the current and voltage during each interval and the complete behavior of the converter. For each of these intervals, first, the equivalent circuit is derived, and the circuit equations are established. Using these equations, a normalized equation is derived, which is plotted on the state-plane to obtain the trajectory and further, the closed-form solution of the converter.

2.3.1 Intervals with State Plane Trajectory

Interval I [$0 < \omega t \leq \Phi$]: The circuit operation begins at $\omega t = 0$ as shown in Fig. 2.6. It is assumed that initially the switches Q7, Q8 are already in conduction and switches Q3, Q4 are turned off. The inductor current is lagging, i.e., negative at the beginning of interval, as shown in Fig. 2.6 (a). Switches Q1 and Q2 are turned on at $\omega t = 0$. C_r and L_r forms a parallel resonant tank as shown in Fig. 2.6 (b) and the tank capacitor voltage v_{cr} appears across the output of the inverter bridge, i.e., $v_P = v_{cr}$. Q7, Q8 continue to conduct and a constant voltage equal to $-V_{out}$ appears across the input of rectifier bridge as shown in Fig. 2.6 (b). A difference voltage $v_{Lr} = v_{cr} + nV_{out}$ appears across the resonant inductor, causing the inductor current to rise with a positive slope. The equivalent circuit can be represented using the differential equations (2.3) and (2.4).

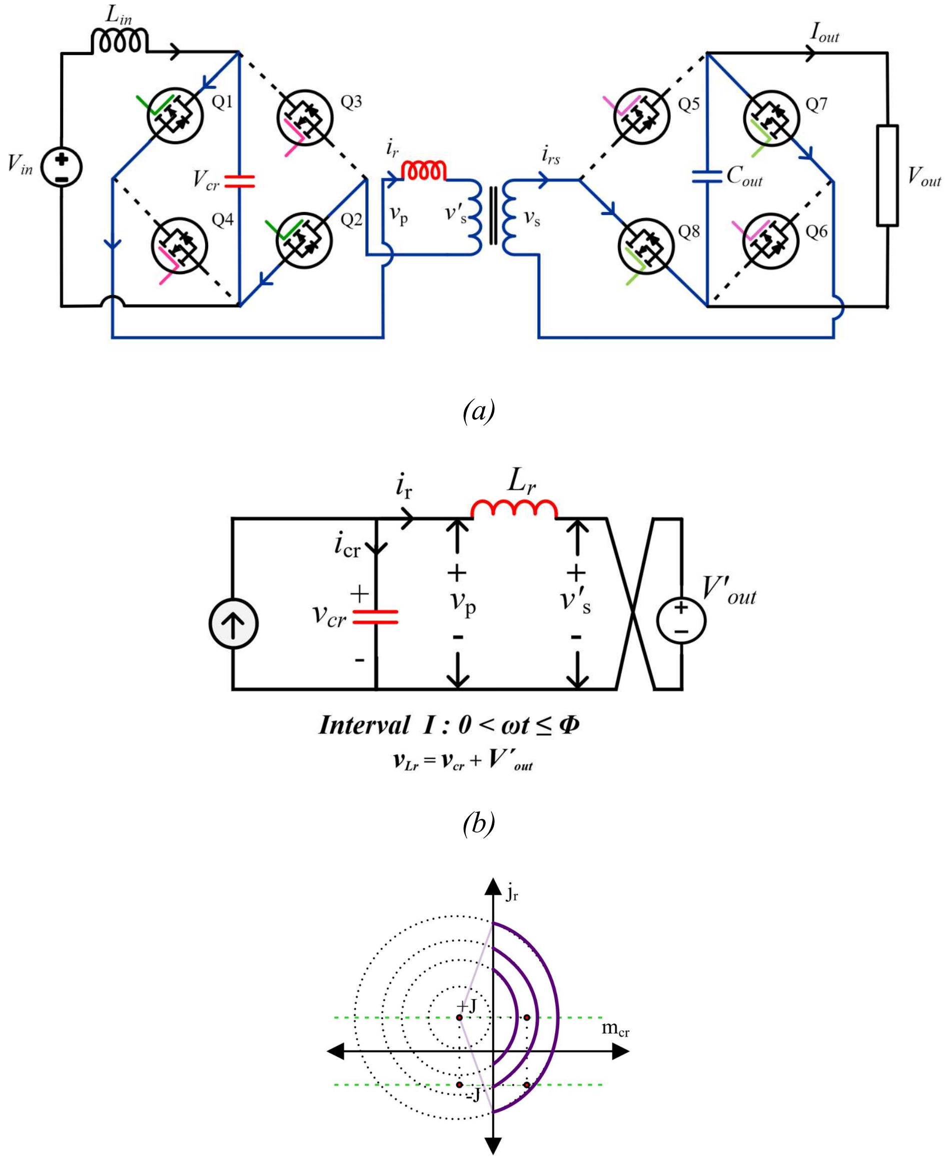

(a)

(b)

(c)

Fig. 2.6 Proposed converter in interval I (a) Circuit with active switches (b) Equivalent circuit (c) State-plane trajectory.

$$L_r \frac{di_r(t)}{dt} = v_{cr}(t) + nV_{out} \tag{2.3}$$

$$C_r \frac{dv_{cr}(t)}{dt} = I_{in} - i_r(t) \tag{2.4}$$

The solution of these differential equations may be represented as in (2.5), (2.6).

$$v_{cr}(t) = (v_{cr}(0) + nV_{out}) \cos \omega_o t + (I_{in} - i_r(0))Z_o \sin \omega_o t - nV_{out} \tag{2.5}$$

$$i_r(t) = \frac{(v_{cr}(0) + nV_{out})}{Z_o} \sin \omega_o t - (I_{in} - i_r(0)) \cos \omega_o t + I_{in} \tag{2.6}$$

The normalized equations of this interval are represented as

$$m_{cr}(t) = (M_{cro} + 1) \cos \omega_o t + (J - J_{ro}) \sin \omega_o t - 1 \tag{2.7}$$

$$j_r(t) = (M_{cro} + 1) \sin \omega_o t - (J - J_{ro}) \cos \omega_o t + \mathrm{J} \tag{2.8}$$

Where, J_{ro} and M_{cro} are the initial current and voltage gain. Using (2.7) and (2.8) the relationship between m_{cr} and j_r could be derived which represents the equation of a circle as can be observed by (2.9). Thus, interval I is a circle with its center $(-1, J)$ and radius $\sqrt{(M_{cro} + 1)^2 + (J - J_{ro})^2}$ in state-plane. The trajectory of interval I is shown in Fig. 2.6 (c).

$$(m_{cr}(t) + 1)^2 + (j_r(t) - J)^2 = (M_{cro} + 1)^2 + (J - J_{ro})^2 \tag{2.9}$$

Interval II [$\Phi < \omega t \leq \pi$]: Fig. 2.7 (a) and (b) represents the proposed converter with active switches and equivalent circuit in interval II, respectively. This interval begins at a phase shift of Φ, when the switches Q1, Q2 of inverter bridge continue to conduct while switches Q7, Q8 of the rectifier bridge are turned off, and Q5, Q6 are turned on. Due to the switch position of rectifier bridge, a positive voltage V_{out} now appears at the rectifier input. The resonant inductor voltage becomes $v_{Lr} = v_{cr} - nV_{out}$. The inductor current continues to rise with a positive slope and attains the peak. Further, as v_{cr} decreases, the current falls with a negative slope. This interval ends at $\omega t = \pi$. The circuit equations are given as (2.10), (2.11)and the solutions are derived in (2.12) and (2.13).

$$L_r \frac{di_r(t)}{dt} = v_{cr}(t) - nV_{out} \tag{2.10}$$

$$C_r \frac{dv_{cr}(t)}{dt} = I_{in} - i_r(t) \tag{2.11}$$

$$\begin{aligned} v_{cr}(t) = {} & (v_{cr}(\phi) - nV_{out}) \cos(\omega_o t - \phi) \\ & + \big(I_{in} - i_r(\phi)\big)Z_o \sin(\omega_o t - \phi) + nV_{out} \end{aligned} \tag{2.12}$$

$$\begin{aligned} i_r(t) = {} & \frac{(v_{cr}(\phi) - nV_{out})}{Z_o} \sin(\omega_o t - \phi) \\ & - \big(I_{in} - i_r(\phi)\big) \cos(\omega_o t - \phi) + I_{in} \end{aligned} \tag{2.13}$$

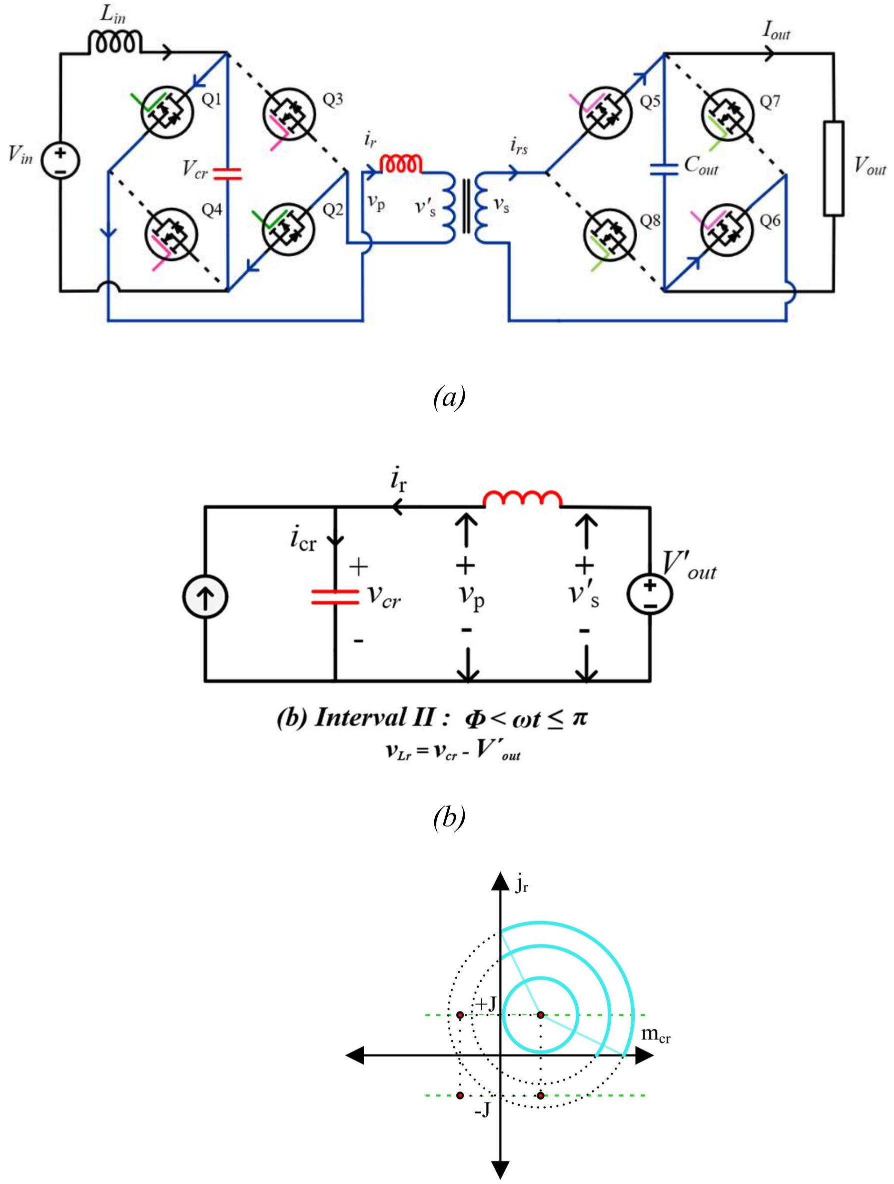

(a)

(b)

(c)

Fig. 2.7 Proposed converter in interval II (a) Circuit with active switches (b) Equivalent circuit (c) State-plane trajectory.

The normalized equations of this interval are represented as (2.14) and (2.15)

$$m_{cr}(t) = \left(M_{cr\phi} - 1\right) cos(\omega_o t - \phi) + \left(J - J_{r\phi}\right) sin(\omega_o t - \phi) + 1 \tag{2.14}$$

$$j_r(t) = (M_{cr\phi} - 1)\, sin(\omega_o t - \phi) - (J - J_{ro})\, cos(\omega_o t - \phi) + J \tag{2.15}$$

where, $J_{r\phi}$ and $M_{cr\phi}$ are the current and voltage gain at *Φ*. Using (2.14) and (2.15) the relationship between M and J is established in (16). It represents a circle with its center

$(1, J)$ and radius $\sqrt{(M_{cr\phi}-1)^2+(J-J_{r\phi})^2}$ in state-plane. The trajectory of interval II is shown in Fig. 2.7 (c).

$$(m_{cr}(t)-1)^2+(j_r(t)-J)^2 = (M_{cr\phi}-1)^2+(J-J_{r\phi})^2 \tag{2.16}$$

Interval III [$\pi < \omega t \le (\pi+\Phi)$]: Fig. 2.8 (a) shows the active switches during interval III. At $\omega t = \pi$, switches Q1, Q2 are turned off, and Q3, Q4 are turned on.

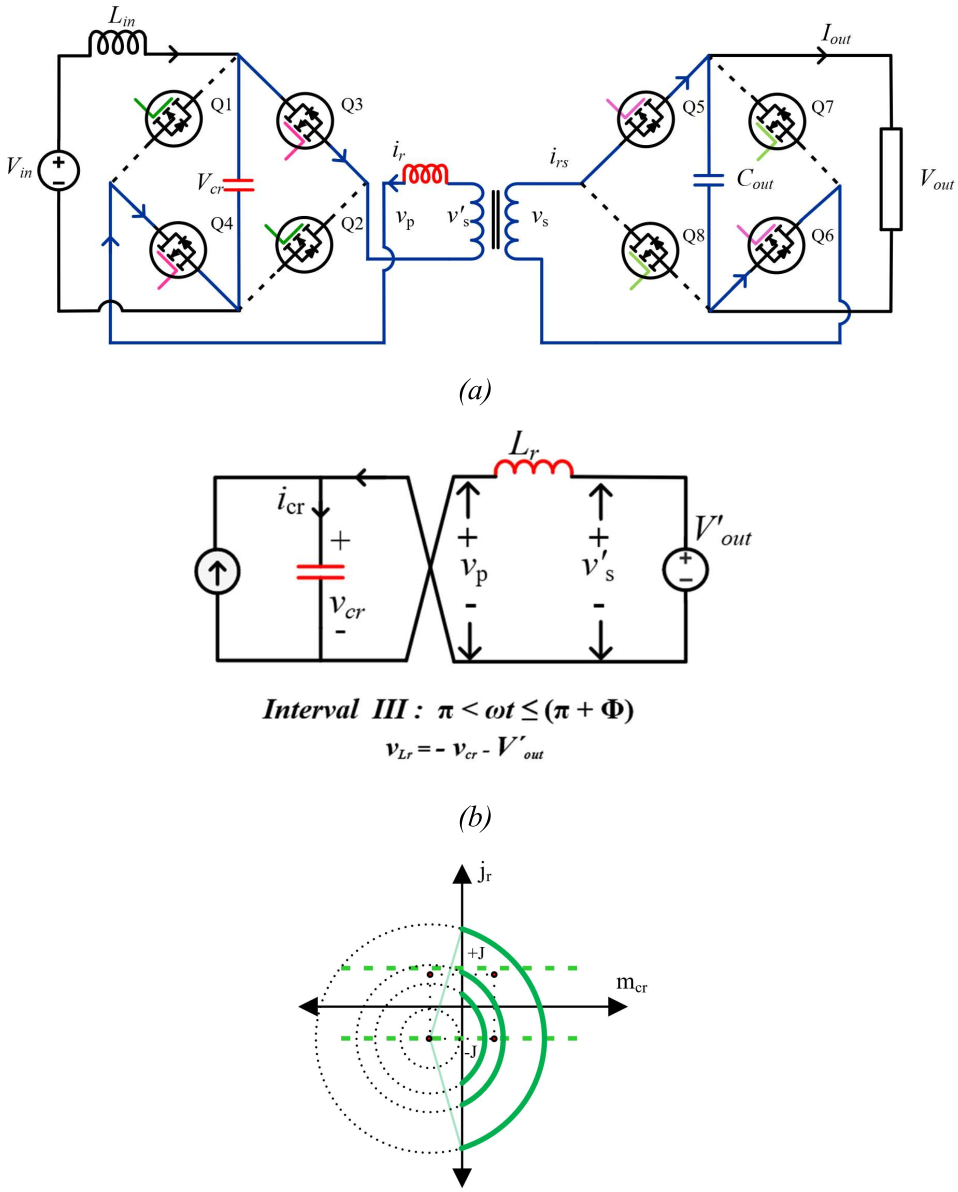

(a)

(b)

(c)

Fig. 2.8 Proposed converter in interval III (a) Circuit with active switches (b) Equivalent circuit (c) State-plane trajectory

The current flowing through Q1, Q2 is transferred to Q3 and Q4, and continues to flow through the antiparallel diodes of Q3, Q4 gradually discharging resonant inductor *L_r*. Q5, Q6 continue to conduct maintaining a positive voltage *V_{out}* across secondary. The equivalent circuit in this interval is shown in Fig. 2.8 (b). Current i_r decreases with a negative slope. Due to the symmetrical operation, the converter operation is similar to interval I, with only the polarities reversed. This implies that $v_P(\pi) = -v_{cr}(\pi) = -v_{cr}(0)$ and $i_r(\pi) = -i_r(0)$. This mode ends when Q5, Q6 is turned off at ωt= π + Φ. Since the operation is similar, the equations are given directly for interval III.

$$L_r \frac{di_r(t)}{dt} = -v_{cr}(t) - nV_{out} \tag{2.17}$$

$$C_r \frac{dv_{cr}(t)}{dt} = I_{in} + i_r(t) \tag{2.18}$$

$$(m_{cr}(t)+1)^2 + (j_r(t)+J)^2 = (M_{cro}+1)^2 + (J+J_{ro})^2 \tag{2.19}$$

The trajectory of interval III is again a circle with center $(-1,-J)$ and radius $\sqrt{(M_{cro}+1)^2 + (J+J_{ro})^2}$. The trajectory is shown in Fig. 2.8 (c).

Interval IV [(π+Φ) < ωt ≤ 2π]: During this interval, switches Q3, Q4 of the inverter bridge continue to conduct Q5, Q6 are turned off and the switches Q7, Q8 are turned on. The active switching circuit with equivalent circuit in interval IV is shown in *Fig.* 2.9 (a) and (b), respectively. Current i_r reaches a negative peak before beginning to rise again with a positive slope. The equivalent circuit equations are given as (20) and it (21). The solution of these equation is given by (22). It represents a circle with center $(1,-J)$ and radius $\sqrt{(M_{cr\phi}-1)^2 + (J-J_{r\phi})^2}$. The conduction interval of one complete switching cycle completes at interval IV and then repeats in every switching cycle. The state plane trajectory is represented in *Fig.* 2.9 (c).

$$L_r \frac{di_r(t)}{dt} = -v_{cr}(t) + nV_{out} \tag{2.20}$$

$$C_r \frac{dv_{cr}(t)}{dt} = I_{in} + i_r(t) \tag{2.21}$$

$$(m_{cr}(t)-1)^2 + (j_r(t)+J)^2 = (M_{cr\phi}-1)^2 + (J+J_{r\phi})^2 \tag{2.22}$$

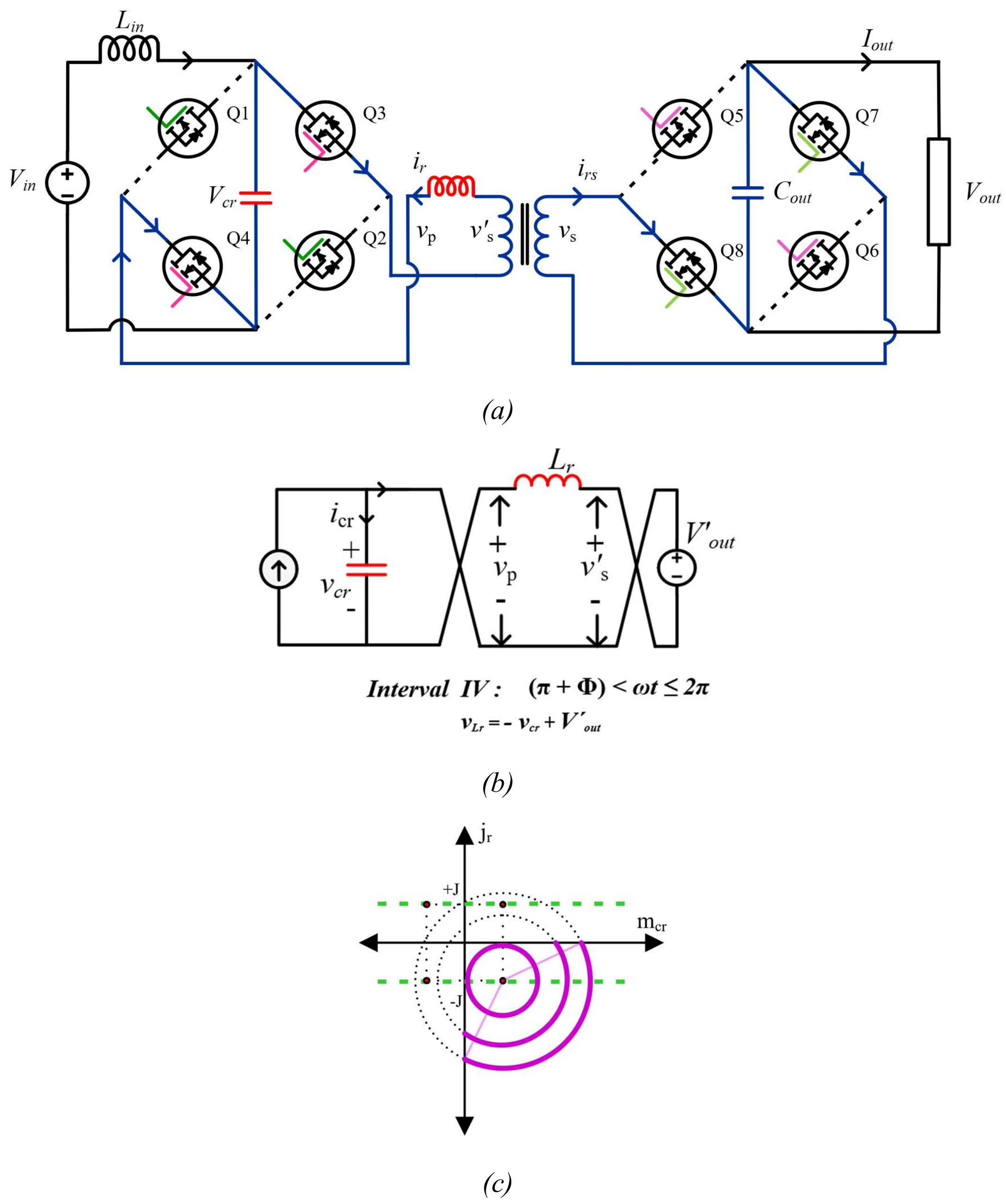

Fig. 2.9 Proposed converter in interval IV (a) Circuit with active switches (b) Equivalent circuit (c) State-plane trajectory.

2.3.1 Closed Form Solution of State Plane Analysis

The composite state plane trajectory of the converter compiling the geometrical solution of all the intervals of operation and their corresponding conducting devices is shown in Fig. 2.10. It is important to note that the resonant capacitor voltage remains positive in all four intervals due to its placement before the switching inverter bridge. This causes the trajectory to remain within the first and the fourth quadrant. Since, the current and voltage of resonant tank possess half wave symmetry, the points a-c and b-d must be equidistant from the origin and always lie on the straight line parallel to current axis as can be seen in Fig. 2.10. The steady-state characteristics of the converter can be obtained by geometrically solving the closed trajectory and result is used in establishing the output gain relation which is otherwise difficult due to the presence of linear and trigonometric terms in the resonant current and voltage expressions.

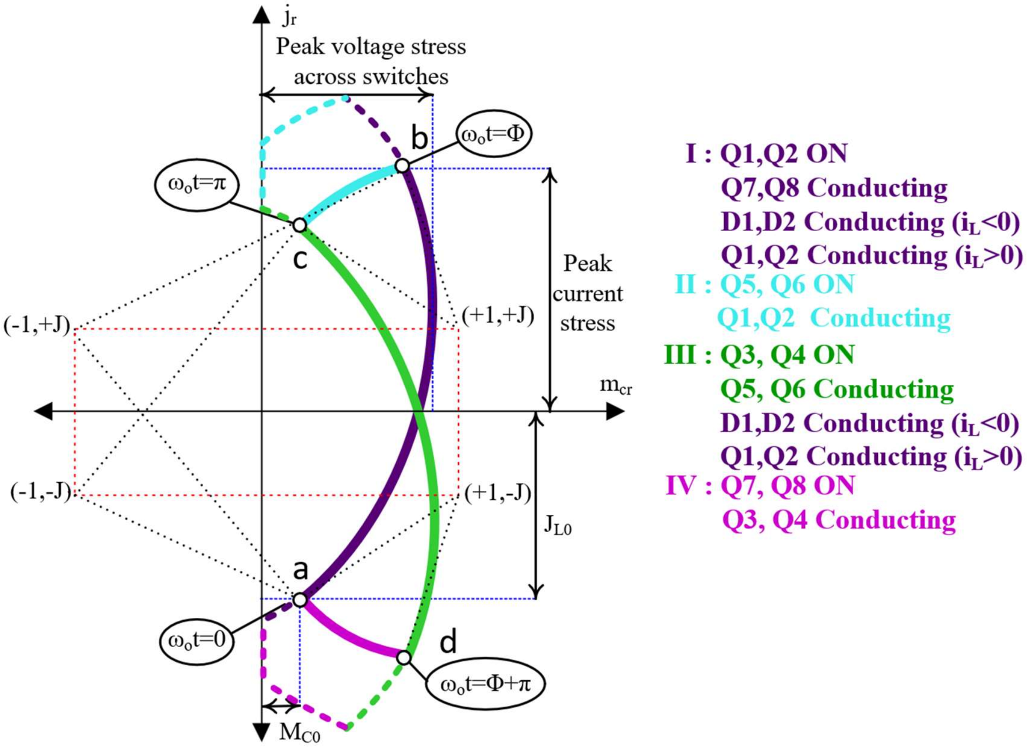

Fig. 2.10 State plane trajectory of the proposed current driven bi-frequency resonant dual active bridge converter.

2.4 Performance Analysis of Proposed Optimal Battery Charger

The converter steady-state output characteristics can be derived by implying the closed state-plane trajectory of Fig. 2.10. The average voltage across resonant capacitor which is equal to the input voltage is given by

$$V_{in} = \frac{2}{T_s}\int_0^{T_s/2} v_{cr}\,(t).\,dt \tag{2.23}$$

From (2.23), a simple relation between converter normalized input voltage and the normalized tank current boundary value $J_{r\phi}$ is found, which is given by,

$$M = \frac{V_{in}}{n\,V_{out}} = \frac{2}{\gamma}\,(\frac{\pi}{2} - \phi + J_{r\phi}) \tag{2.24}$$

Utilizing the state-plane trajectories derived in the previous section, the relationship between phase shift angle ϕ with respect to half period angular length γ to determine the normalized current and the normalized voltage equation of the converter is established as (2.24).

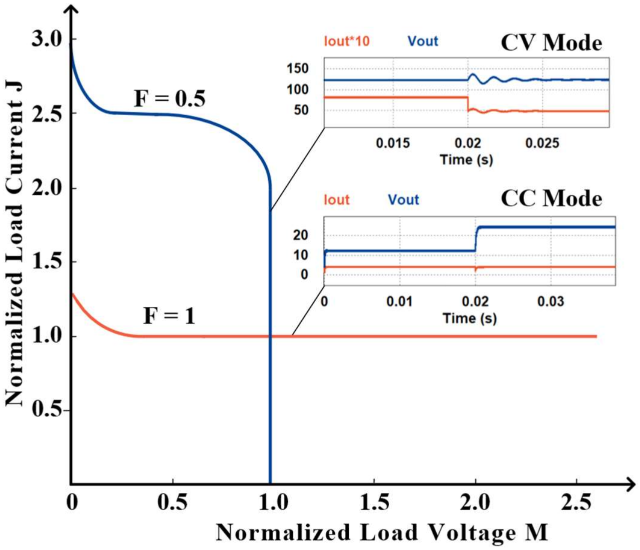

Fig. 2.11 Output characteristics of the equivalent parallel resonant converter plotted on the normalized voltage current (M-J) plane.

Normalized Current:

$$\phi = sin^{-1}\left(cos\frac{\gamma}{2} + J\ sin\frac{\gamma}{2}\right) \tag{2.25}$$

Normalized Voltage:

$$M = \frac{2}{\gamma}\left(\left(\frac{\pi}{2} - \phi\right) - \frac{cos\,\phi}{cos\frac{\gamma}{2}}\right) \tag{2.26}$$

The desired closed form solution of the steady state characteristics for the proposed converter is given by (2.26). For a given load current and operating frequency, the output voltage of the converter can be calculated using (2.26). Using (2.25) and (2.26) the M-J characteristics of the converter is plotted to obtain the converter response with variation in frequency and is shown in Fig. 2.11.

2.4.1 CC-CV Behavior: The M-J Characteristics of Proposed Charger

The variation of load characteristics with frequency in the normalized output plane of the equivalent parallel resonant converter is plotted in Fig. 2.11. The intersection of plotted M-J characteristics with the M-axis gives the tank open circuit voltage and, similarly, the intersection of the characteristic with J axis gives the tank short circuit current. At resonant frequency, the inductive reactance offered by the leakage inductance L_r (which is a part of this resonant tank) becomes equal to the capacitive reactance offered by input film capacitor C_r. Therefore, a situation arises where there is no damping element in the tank circuit leading to relatively large tank open circuit voltage. In other words, the point of intersection on M-J characteristics for operation at resonance frequency (F = 1) moves far away on the M-axis, leading to a characteristics parallel to M-axis. This is reflected in Fig. 2.11. It can be clearly inferred that at resonant frequency, the output voltage of the converter varies when the load resistance is varied, whereas the output current remains constant.

On the contrary, the J-axis intercept or the short-circuit current varies inversely with the operating frequency. This is because during short-circuit, the only impedance existing in the network is the inductive impedance, which decreases with the decrease in frequency. Thus, allowing higher value of current to flow through the circuit. Due to the said property, the converter load characteristics becomes a vertical line with voltage gain constant at $M=1$, making it a voltage source. The simulation results corresponding to each of the operating frequency is shown in Fig. 2.11, which verifies the converter CC-CV behavior.

2.4.2 Charger Output in CC and CV Mode

In CC mode of operation, the normalized current becomes constant and is given by

$$J = \sin\phi \tag{2.27}$$

Further, the load voltage and load current using above equations are given by,

$$I_{out} = \frac{n\,V_{in}}{Z_o}\,sin\,\phi \tag{2.28}$$

$$V_{out} = \frac{V_{in}\,R_L}{n\,Z_o} sin\,\phi \tag{2.29}$$

where, R_L= Load resistance connected at the output

Similarly, in the CV mode of operation, the normalized voltage gain of the converter becomes constant and is given by

$$M = \frac{V_{in}}{n\, V_{out}} = 1 \tag{2.30}$$

$$I_{out} = \frac{V_{out}}{R_L} \tag{2.31}$$

The equations verify that the behavior observed in the load characteristics.

2.5 Design of the Converter

A 1 kW experimental prototype operating at 100 kHz and 50 kHz is taken as an example to select the main parameters of the design consideration. The specification considered for the prototype are as follow: $V_{in} = 150\, V$, $V_{out} = 95\, V$, resonant frequency, $f_r = 100\, kHz$.

2.5.1 Transformer Turn Ratio

The turns ratio of the transformer should be designed to make sure that the power and voltage can be regulated within the entire ranges of the desired battery voltage (V_{out}) and input voltage (V_{in}). However, as the maximum voltage across the output of the converter appears during CV mode, the turn-ratio should be selected accordingly and is defined as $V_{out-max}$. Using $M = 1$ in (2.30), the turn ratio of the transformer (n) can be found by

$$n = \frac{V_{in}}{V_{out-max}} \tag{2.32}$$

Considering an input voltage of $V_{in} = 150\, V$, and maximum battery voltage to be 95 V, a turn ratio of 1.58 was obtained, and the transformer was designed suitably for 16:10 turns.

2.5.2 Design of Magnetics Component

The selection of the switching frequency is often related to the design process of the magnetic components. A higher switching frequency would allow small and compact design. Also, from (2.6) and (2.13), it can be seen that the current flowing through the leakage inductance of transformer is inversely proportional to the characteristic's impedance Z_o of the tank. In other words, to allow the same amount of load current, a higher switching frequency would require smaller inductance value. Therefore, considering the maximum current required in the CC mode, the magnetics for the proposed converter is designed for higher switching frequency of operation, which is the resonant frequency. Further, in CV mode of charging, the battery internal resistance becomes very high and therefore the load current sharply decreases to a very low value known as trickle charging. This reduces the current stress during CV mode as can also be inferred from Table 2.2. Therefore, the same inductor that is designed for CC mode will work fine for CV mode as well, while allowing a reduced current through the inductor.

Table 2.2 Current Stress Analysis of Proposed Converter

CC mode f_s *= 100 kHz* *Vin =150 V*

P_{out} (W)	V_{out} (V)	I_{out} (A)	$I_{r\text{-}peak}$ (A)	$I_{rsec\text{-}peak}$ (A)
623.8 W	60.5 V	10 A	9.6 A	16.1 A
724 W	71.7 V	10 A	10.5 A	16.8 A
921.6 W	92 V	10 A	11.28 A	19.11 A

CV mode f_s *= 50 kHz* *Vin =150 V*

P_{out} (W)	V_{out} (V)	I_{out} (A)	$I_{r\text{-}peak}$ (A)	$I_{rsec\text{-}peak}$ (A)
659.8 W	92 V	7.15 A	9.2 A	14.46 A
537.13 W	92 V	5.79 A	7.8 A	12.23 A
346.6 W	92 V	3.71 A	5.4 A	8.16 A

Therefore, considering I_{out} as the current during CC mode, and using (2.28), the tank characteristic impedance can be found as

$$Z_o = \frac{n\, V_{in}\, \sin\phi}{I_{out}} \tag{2.33}$$

As the value of Z_o is known, using $Z_o = \sqrt{L_r/C_r}$ and $\omega o = 1/\sqrt{L_r C_r}$, the required leakage inductance (L_r) can be found to transfer the desired power. Considering ϕ = 80°, $and\, f_o = 100\ kHz,\ Z_o$ was found to be 23.5 Ω and a leakage inductance of $L_r = 37.40\ uH$.

2.5.1 Selection of Input Capacitor

The selection of type of capacitor significantly effects the reliability of converter, which is of prime importance in charger applications. The input capacitor is made to resonate with the leakage inductance of the transformer and value of this capacitor is calculated in accordance to the resonant frequency ω_o. The higher switching frequency results in a smaller capacitance value as compared to the conventional DAB filter capacitor. It is due to the resonance that the capacitance value could be reduced and the electrolytic capacitor could be replaced with the metal film capacitor which resulted in reduction in the size of capacitor (capacitance value and physical dimension), reduction in cost and better reliability of the converter [29]. This presents an opportunity of achieving a lower cost and higher power density dc-link design with metal-film in high ripple current applications, like the case in electric vehicles.

Based on the value of L_r the capacitance C_r is found to be 67.2 nF. In order to design the resonant tank based on the above values of inductor and capacitor, the capacitor is chosen first as per the commercial availability. The closest available value of capacitance is chosen to be 68 nF and accordingly the transformer is designed to limit the values of leakage and mutual inductances. The selected rating of the capacitor is 68 nF, 650 V and the transformer leakage inductance is found to be 36.5 μH.

2.5.2 Selection of Input Inductor

The selection of input inductor depends on the maximum current flowing through it and the maximum allowable ripple current. The maximum input current is drawn from the source during the CC mode as the maximum current is delivered by the converter during this mode. Hence, input inductor value is designed considering the input current drawn during CC mode.

From the circuit operation, it is known that the average current supplied by the input I_{in} is given by (2.34). The input inductance can be calculated from the relationship between change in input current with respect to time and voltage at the input,

$$L_{in}\frac{\Delta I_{in}}{\Delta t} = V_{in} \tag{2.34}$$

Where Δt is the time duration for which the switches Q1, Q2 are tuned on, and ΔI_{in} is the allowed ripple in the input current which depend on the specific application. In this case, the allowed % ripple was taken to be 20%. Considering the above equation, the value of input inductance was found to be 2.6 mH.

2.6 Experimental Verification

To validate the concept of CC-CV charging using current-driven bi-frequency resonant dual active bridge converter, a scaled-down 500 W laboratory prototype of the converter is developed. The selected components and their values are shown in Table 2.3. The experimental setup photograph is shown in Fig. 2.12. It is to be noted that the battery behaves as a variable resistance during charging. Therefore, a varying resistive load is used to emulate the behavior of the battery and obtain the experimental results.

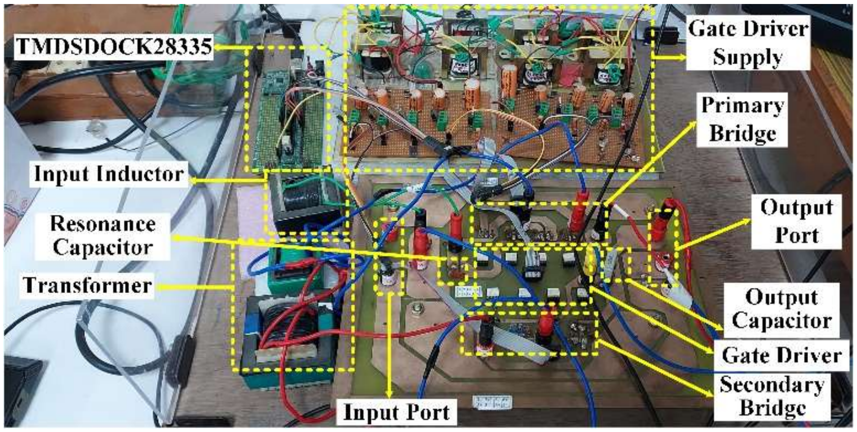

Fig. 2.12 Photograph of the experimental prototype

Table 2.3 Component values used in converter design

Component	Symbol	Part/ Value
Microprocessor		TMS320F28335
MOSFET	**Q1-8**	FCP099N65S3
Gate Driver		FOD3182
Inductor	$\mathbf{L_{in}}$	2.6 mH
Capacitor	$\mathbf{C_{out}}$	235 µF
Turn ratio	**N**	16:10
Leakage Inductance	$\mathbf{L_r}$	36.5 µH
Capacitor	$\mathbf{C_r}$	B32671P6683K000/68 nF
Resonant Frequency	$\mathbf{f_r}$	100 kHz
Switching Frequency	$\mathbf{f_s}$ **(CC)**	100 kHz
	$\mathbf{f_s}$ **(CV)**	50 kHz

2.6.1 Steady State Performance of the Proposed Charger

The current driven bi-frequency resonant dual active bridge converter has been tested for both CC and CV modes and the steady state results are presented in Fig. 2.13 and Fig. 2.14. where it can be observed that the inverter bridge output at primary of the transformer is a resonant voltage which appears across switches of inverter bridges as $V_{DS,Q1}$, and rectifier bridge voltage that appears across the transformer secondary is a square wave voltage, also appearing across the rectifier bridge switches as $V_{DS,Q5}$.

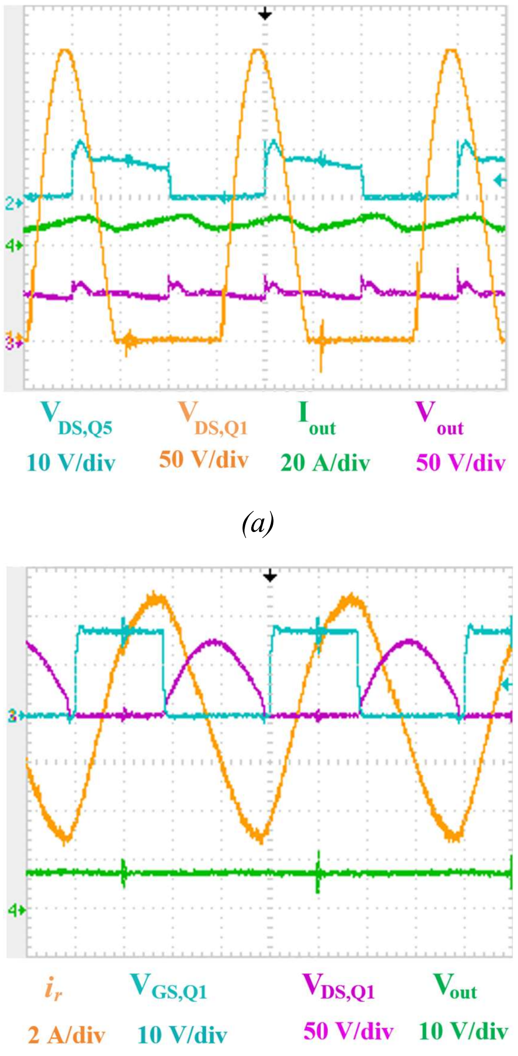

(a)

(b)

Fig. 2.13 Steady state results of proposed converter in CC mode (a) V_{DS} of Q1 and Q5 with V_{out}, I_{out} (b) V_{GS} and V_{DS} for Q1, with i_r and V_{out}.

Fig. 2.13 (a) and (b) shows the steady state results when the converter is operated in CC mode with switching frequency equals to the tank resonant frequency, i.e., $f_s = 100$ kHz.

Fig. 2.13 (a) represents the inverter bridge switch voltage $V_{DS,Q1}$, rectifier bridge switch voltage $V_{DS,Q5}$, load current I_{out} and load voltage V_{out} for output power $P_{out} = 480.6$ W of the converter. Fig. 2.13 (b) shows, voltage across inverter switch $V_{DS,Q1}$, gate pulse $V_{GS,Q1}$, resonant inductor current i_r at the transformer primary and load voltage V_{out}.

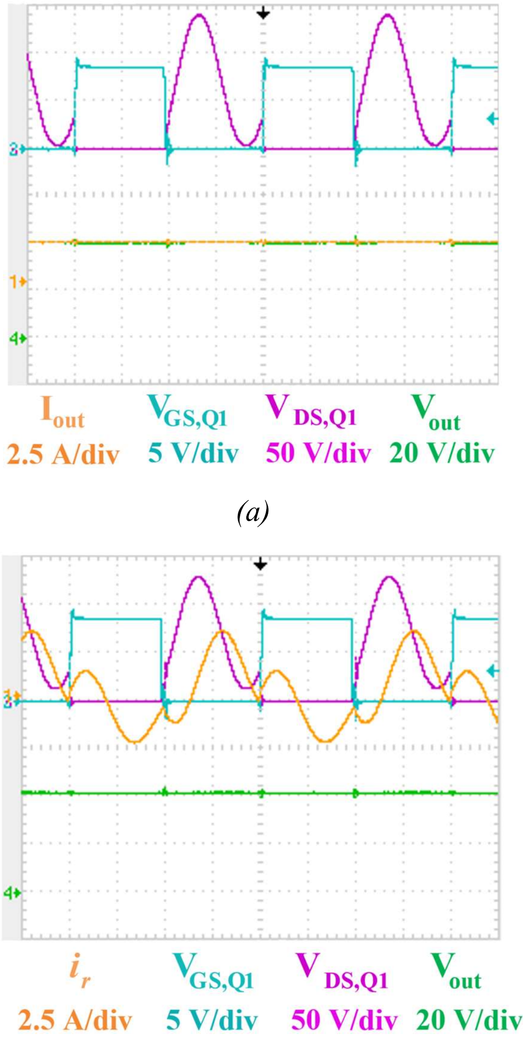

(a)

(b)

Fig. 2.14 Steady state results of proposed converter in CV mode (a) V_{DS} V_{GS} for Q1 with I_{out} and V_{out} (b) V_{DS} $V_{GS,Q1}$ with i_r and V_{out}.

Fig. 2.14 (a) and (b) shows the steady state waveforms when the converter operates at switching frequency equals to half the tank resonant frequency, i.e., $f_s = 50$ kHz, to behave as a voltage source for CV operation. Fig. 2.14 (a) represents the inverter bridge switch voltage $V_{DS,Q1}$, rectifier bridge switch voltage $V_{DS,Q5}$, load current I_{out} and load voltage

V_{out}. Fig. 2.14 (b) shows resonant inductor current i_r flowing through transformer primary side. The measured waveforms verify the operation described in earlier section.

Fig. 2.15 (a) shows the current stress across the primary switches when delivering a load of 48 V, 10 A in CC mode of operation. Fig. 2.15 (b) shows the current stress across the primary bridge switches when delivering 48 V, 2 A in CV mode. This verifies the current stress will be within limits in CC and CV mode for the magnetics to be designed at higher resonant frequency.

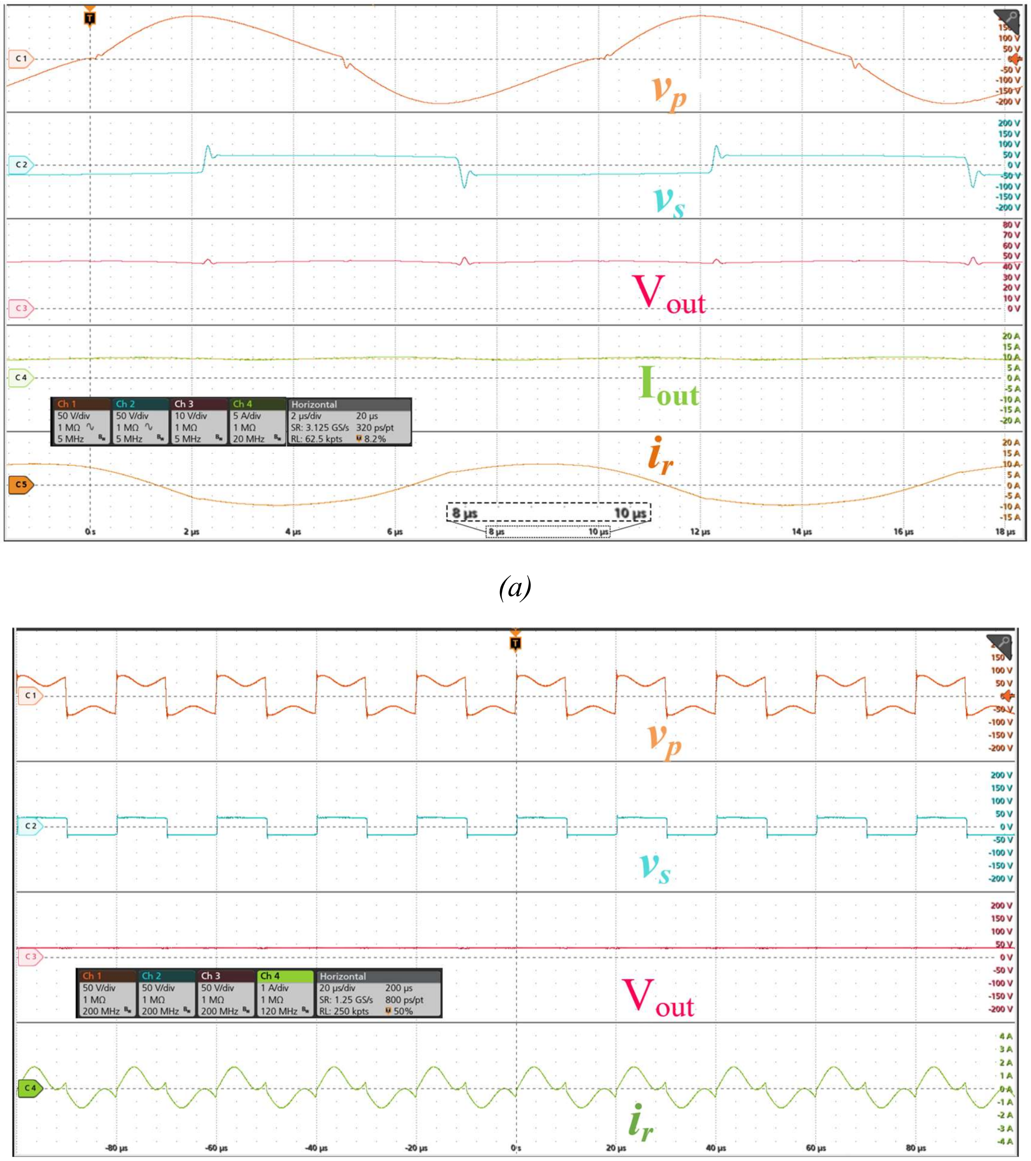

(a)

(b)

Fig. 2.15 (a) Experimental results to demonstrate the current stress in CC mode, with load of 48 V, 10 A (b) Experimental results to demonstrate the current stress in CV mode, with load of 48 V, 2 A

2.6.2 Soft Switching Performance

Fig. 2.16 shows the soft switching achievement of inverter and rectifier bridge switches in different operating conditions. The resonant tank capacitor voltage appears across the inverter bridge switches. Thus, assisting the soft switching transition by decaying the switch voltage to zero before the application of gate pulse. This is shown in Fig. 2.16 (a) for CC mode of operation. $V_{DS,Q1}$ becomes zero before $V_{GS,Q1}$ is applied thus, ensuring zero voltage switching (ZVS) of the inverter bridge switch Q1. Fig. 2.16 (b) shows the switching transition for inverter and rectifier bridge when operating in CV mode.

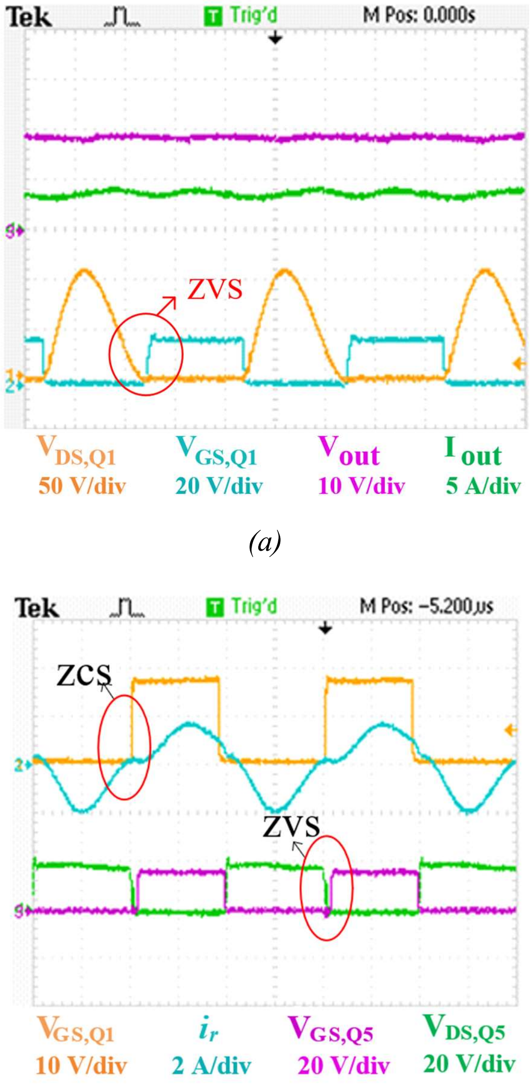

(a)

(b)

Fig. 2.16 (a) ZVS turn-on of the inverter switches Q1 when operating in CC mode. (b) ZCS turn-on of Q1 switches, ZVS turn-on of Q5 in CV mode.

i_r, the resonant inductor current flowing through switch is zero at the instant switch is turned on, thus ensuring zero current switching (ZCS) of inverter bridge switches. For the rectifier bridge, the switch voltage $V_{DS,Q5}$ reaches zero before Q5 is turned on, thus confirming ZVS of rectifier bridge switches.

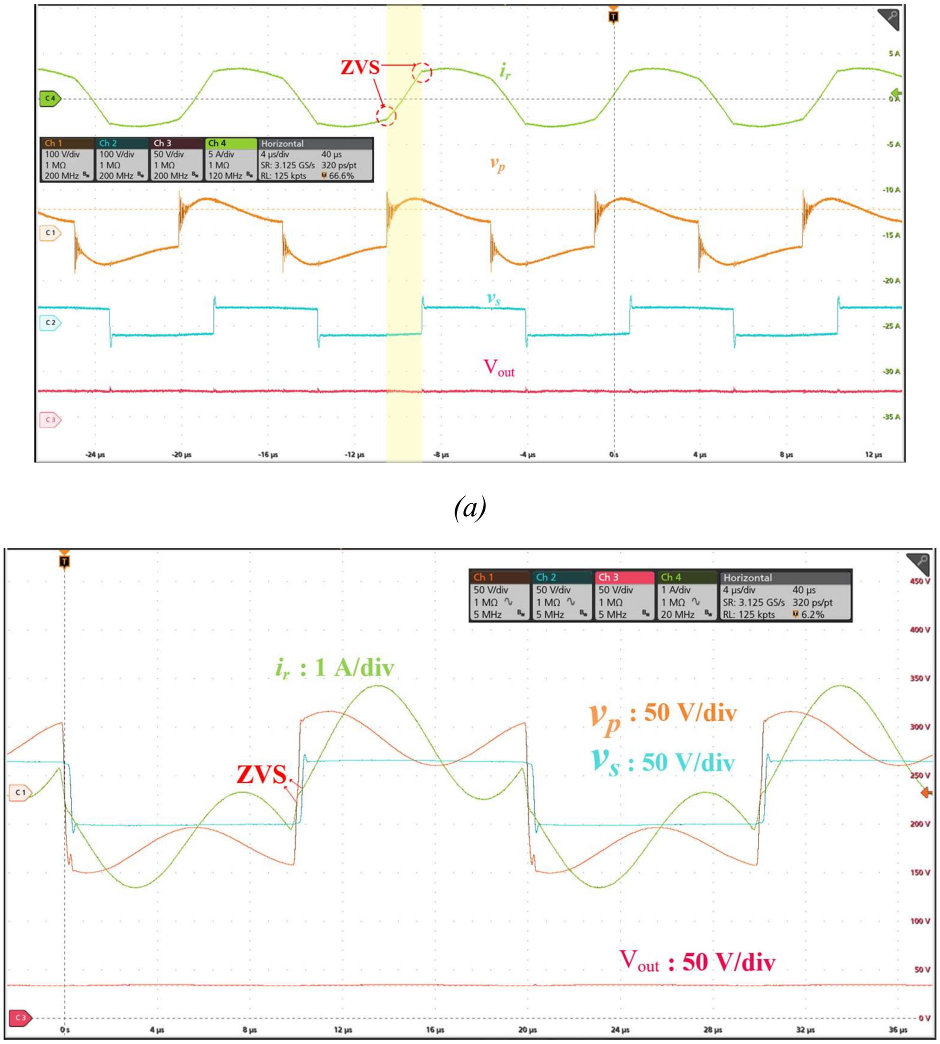

(a)

(b)

Fig. 2.17 (a) ZVS turn-on of the inverter switches and ZVS turn-on of rectifier switches when operating in CC mode. (b) ZCS turn-on of inverter switches, ZVS turn-on of rectifier switches in CV mode.

Fig. 2.17 (a) shows the achievement of ZVS turn-on for all inverter bridge switches as current through switch is negative during turn-on, confirming anti-parallel diode conduction or ZVS turn-on. Similarly, i_r is negative at the instant of turning on of switches from rectifier bridge that confirms ZVS turn-on. Fig. 2.17 (b) shows the current i_r is zero at turn-on of inverter bridge switches showing ZCS turn-on. Whereas i_r is positive at rectifier bridge turn-on confirming ZVS operation. In addition, the inverter bridge switches always undergo near zero turn-on. Thus, imparting higher efficiency to the converter in CV mode. Table 2.4 presents an efficiency analysis of the converter for varying load. It is observed that soft-switching is achieved for entire range of load power and the efficiencies are tabulated.

Table 2.4 Efficiency Analysis of the converter

Mode of operation	**Output Power (W)**	**Output Voltage (V)**	**Output Current (A)**	**Efficiency %**
CC	405.4	40.26	10.2	96.10
	623.8	61.17	10.19	96.18
	725.5	71.2	10.18	96.54
	921.6	91.07	10.11	96.52
Mode of operation	**Output Power**	**Output Voltage**	**Output current**	**Efficiency %**
CV	430.6	92.8	4.64	97.58
	535.9	92.5	5.78	98.47
	658.42	92.5	7.11	98.79
	844	91.8	9.18	98.35

2.6.3 Dynamic Performance of the Proposed Charger

The proposed converter, when operated at resonant frequency gives constant output current irrespective of the perturbance or variation in load resistance, similarly it gives constant output voltage at half of the resonant frequency. To emulate the battery behavior during charging, dynamic waveform with load step-up and step-down is shown in Fig. 2.18 (a), (b) and Fig. 2.19 (a), (b) for CC and CV mode, respectively. I_{out}, the load current remains constant as load voltage V_{out} changes for CC mode and it applies vice-versa for CV mode.

Fig. 2.18 (a) and (b) shows the load transition waveform when the converter is operated in CC mode at switching frequency equals to resonant frequency i.e., 100 kHz. In Fig. 2.18 (a) the load current remains constant at 1.52 A as the load current observes a change of 42.8%. The change in rectifier voltage reflects the change in load voltage while the inverter resonant voltage remains constant. Fig. 2.18 (b) represents that the output current remains constant at 7.28 A for 100% change in load voltage.

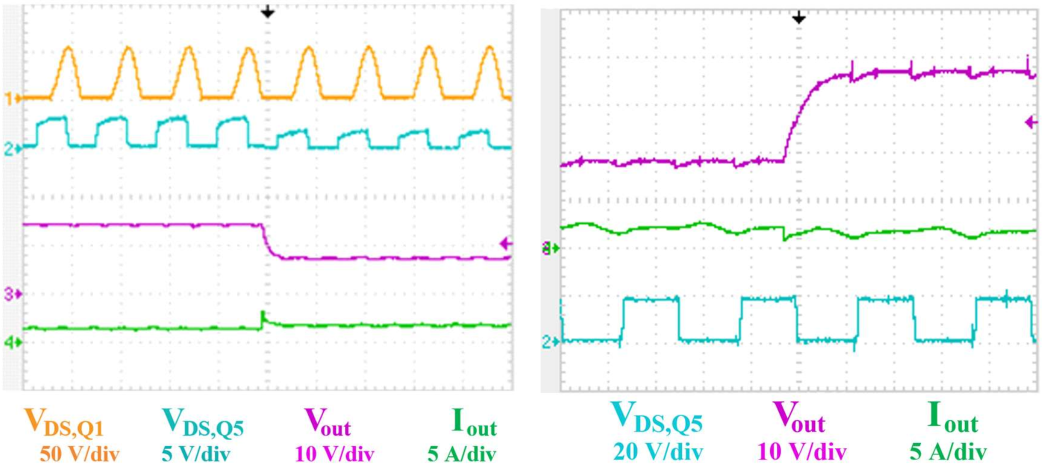

(a) *(b)*

Fig. 2.18 Dynamic response of the proposed converter in CC mode (a) 48% change in load voltage (b) 100% change in load voltage.

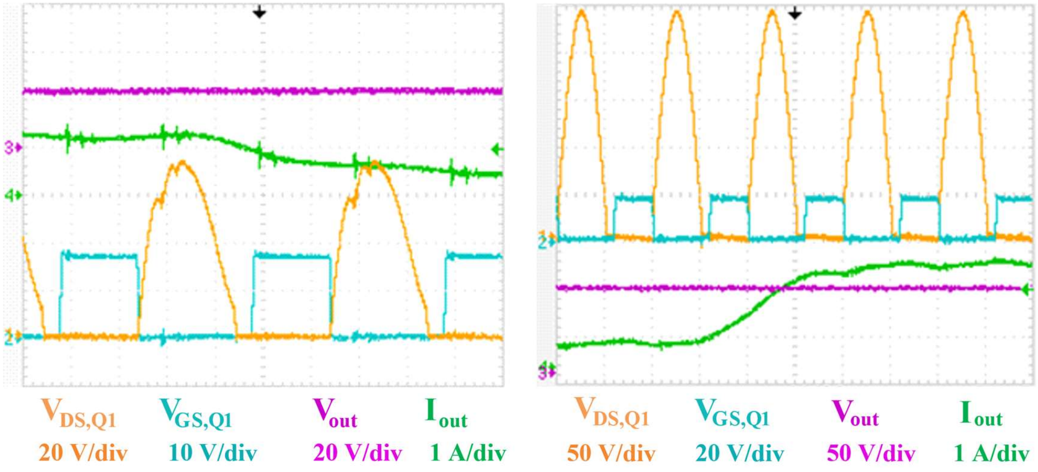

(a) *(b)*

Fig. 2.19 Dynamic response of the proposed converter in CV mode (a) 66.67% change in load current (b) 200% change in load current.

Fig. 2.19 (a) and (b) shows the dynamic behavior of converter when operated at half the resonant frequency, i.e., 50 kHz. It may be observed that the load current decrease with a change of 66.67% while load voltage remains constant at 23.6 V in Fig. 2.19 (a). Fig. 2.19 (b) shows that for 200% change in load current the load voltage remains constant at 89.4 V, thus confirming the CV behavior of the converter when operated at half the resonant frequency.

2.6.4 Transition from CC to CV Mode

For CC-CV battery charging operation the transition between the modes is achieved by sensing the output voltage of the converter, thus making the control strategy simple. The operation of the converter is such that, the converter is initially operated at switching frequency equals to resonant frequency ($f_s = f_r$) to operate in CC mode. A constant current is fed to the battery and the battery terminal voltage rises from its initial voltage to a reference value, which is the standard charge voltage (full voltage) of the battery as specified by the battery manufacturer.

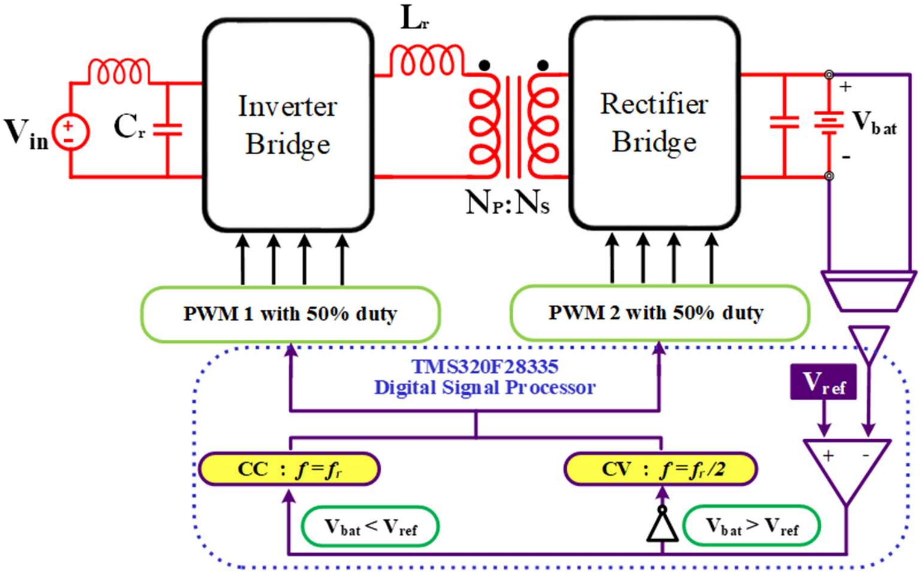

Fig. 2.20 Block diagram representation of sensing and control technique used for CC-CV implementation of proposed Current-Driven Bi-Frequency Resonant Dual Active Bridge Converter.

As soon as the output voltage reaches this reference value, switching frequency is changed to half of the resonant frequency ($f_s = f_r/2$). At this operating point, the converter operation transits to constant voltage mode, where battery charging process enters into CV mode. The charging continues at constant voltage and the battery current deceases to a very low value (trickle charging) due to sharp rise in battery internal resistance. The

CC-CV charging curve is shown in Fig. 2.3 (a). In order to achieve such transition with proposed converter, the control logic used is also depicted in Fig. 2.20.

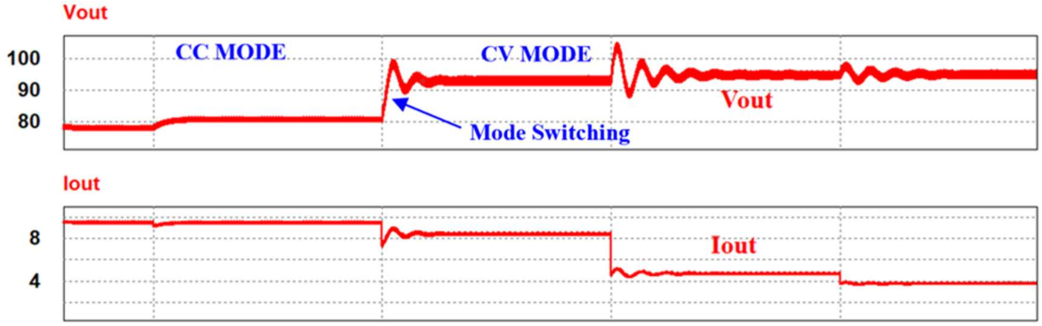

Fig. 2.21 Simulation results to present the stable operation of converter in CC mode, during transition from CC to CV, and during CV mode.

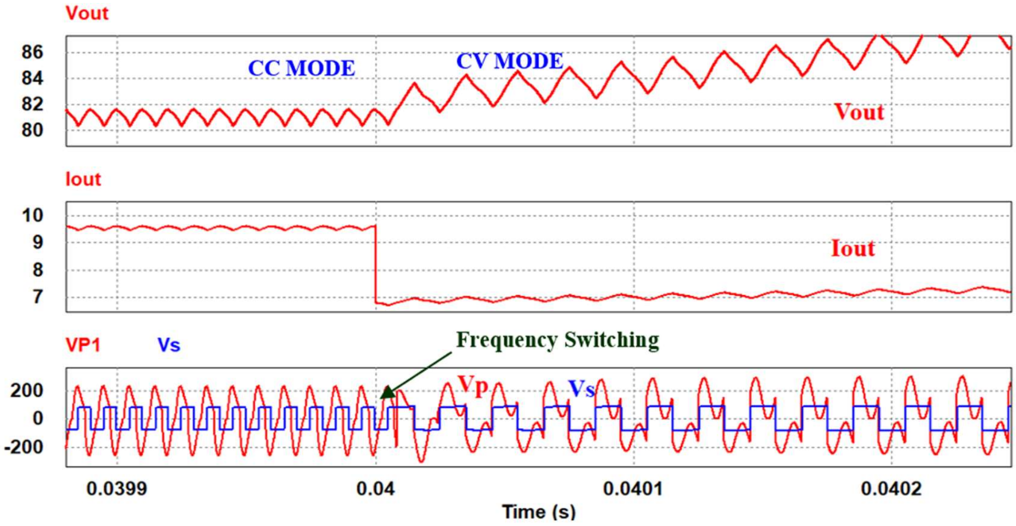

Fig. 2.22 Zoomed view of simulation results to present the transition from CC to CV mode.

Fig. 2.21 shows the converter is initially charging in CC mode with terminal voltage increasing. The mode switches at the reference voltage and charging transits in CV mode. The results show a stable converter operation during CC-CV charging and a smooth transition from CC to CV mode. Further, to validate the performance of converter during mode switching the zoomed view of transition instant is presented in Fig. 2.22. It shows smooth transition from CC to CV mode.

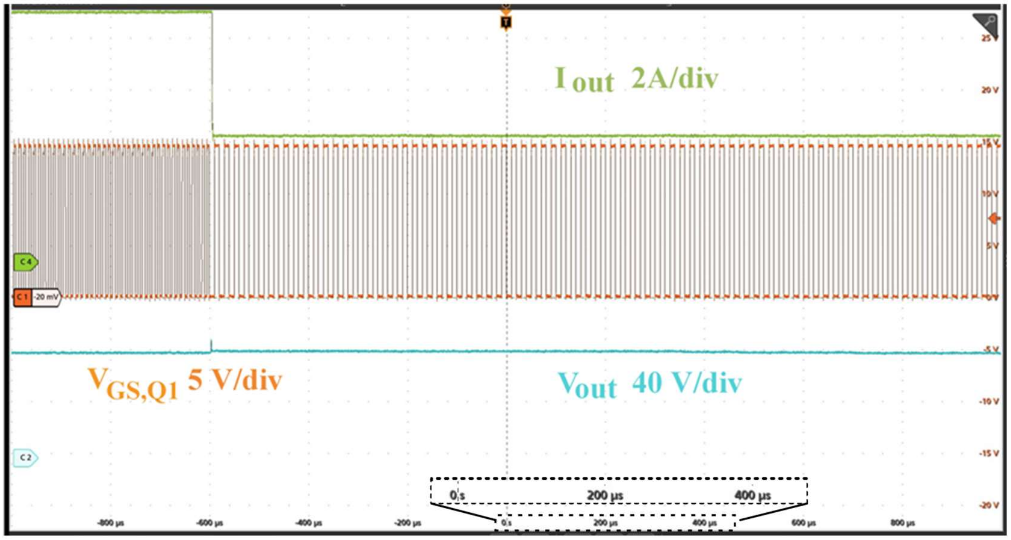

Fig. 2.23 Experimental results to demonstrate the transition of converter operation from CC to CV mode.

The experimental results demonstrating the transition from CC to CV mode are shown in Fig. 2.23. During CC mode, at the beginning of charging, the battery internal resistance is assumed to be 7.5 ohms and the internal resistance of the battery at the end of charging corresponding to CV mode is considered to be 30 ohms. It may be observed that with slight increase in voltage the frequency switching occurs and the current sharply reduces. Thus, verifying the converter operation in CV mode after transitioning form CC mode.

2.6.5 Cost Comparison with Existing Literature

Past literature suggests application of modulation techniques such as SPS, DPS, TPS, EPS, PFM, etc. to enhance the performance of the DAB converter for CC-CV charging. In another work, authors utilized extended phase shift modulation (EPS) for charging in CC mode while DPS control was utilized for voltage regulation in CV mode. However, it is noteworthy that for all of the above reported control methods, the power transfer is mainly controlled by three independent control variables, which are: each of the bridges' inner phase shift ratios (which describes the pattern of switching in one bridge with respect to its other switch) and the phase shift ratio between the two bridges (which describes the pattern of switching of one bridge with respect to the other bridge switches).

With the increase in the number of adjustable control variables, the designed model for decision making becomes complex. Because, it varies with different time intervals, different operation states and different phase shift methods. Thus, the establishment of a model while handling large number of control variable for a decision making becomes very difficult. Further, the calculation of parameters becomes hard and confusing, and therefore the controller design process is considered complex [37], [38], [124].

In addition, to optimize the selection of these three independent control variables, the optimization schemes are based on mathematical analysis with different optimization goals, such as optimized efficiency [125], minimizing conduction loss. These optimizations need complex power calculation, working mode classification and may also highly depend on the system parameters [126]. The discussed evidences verify the complexity of existing modulation techniques. Whereas, the proposed converter uses a single phase-shift control which simplifies the modulation technique.

Further, in addition to the modulation techniques, the DAB control requires dedicated control algorithms for CC-CV charging implementation to regulate its output effectively. These control techniques include linear proportional integral (PI) controllers, feedback controller, feed-forward controller, Model predictive controller (MPC), and sliding mode controller (SMC) and moving discretized control set model-predictive control (MDCS - MPC). These control technique algorithms have their own complexity and requirements.

Table 2.4 Comparison of DAB Control Techniques For CC-CV Charging Implementation

	Modulation technique	Type of controller	Complexity	Cost
[35]	EPS (PI)+ DPS (MPC)	PI + MPC	High	High
[36]	DPS (PI)	PI*2	Low	Medium
[37]	TPS	MDCS-MPC	High	High
[38]	PFM + PSM	PI *2	Medium	Medium
[39]	SPS	SMC	Low	Low
Proposed Converter	SPS	None	Low	Low

A cost comparison of the proposed converter for the desired CC-CV operation with the existing control strategies utilizing dedicated modulation technique to achieve CC-CV charging of batteries is performed. The conclusions are presented in Table 2.4. The implementation cost of any control scheme to achieve a desired output includes costs of voltage and current sensors, cost of ADC and microprocessor computational power for the method to be properly functioning. The required microprocessor computational power is related to complexity and multiple sensors. The low-cost methods are those with low complexity and single sensor. The proposed converter uses single phase shift control and a simple logic to switch from CC to CV mode by sensing only one output, i.e., the load voltage of the converter. Hence, from the above discussion, it may be clearly interpreted that the proposed converters operation to perform CC-CV charging is simple owing to its low complexity and has low cost due to fewer number of sensing parameters, that is affected by the required sensor and ADC cost.

2.6.1 Efficiency Analysis of the Proposed Converter

A comparative analysis of the proposed converter with existing competitive topologies is performed and the results are given in Table 2.5. The comparison is made on the basis of reference output power for full load and 40 % load (i.e., 200 W and 500 W), when the input voltage is of 150 V and load terminal voltage of 48 V. The current stress on the low voltage side is also tabulated along with the switching and conduction losses in each of the case. From the tabulated results, it can be clearly inferred that the proposed converter gives improved efficiency at both full load and 40% load compared to the existing topologies. The improvement in efficiency is primarily due to the elimination of turn-on switching losses in both primary and secondary bridge switches and reduced conduction losses as a result of reduced inductor current. The proposed converter uses single phase shift control and a simple logic to switch from CC to CV mode by sensing only one output, i.e., the load voltage of the converter. Hence, from the above discussion, it may be clearly interpreted that the proposed converters operation to perform CC-CV charging is simple owing to its low complexity and has low cost due to fewer number of sensing parameters, that is affected by the required sensor and ADC cost.

Table 2.5 Efficiency Comparison of Proposed Current-Driven Bi-Frequency Resonant DAB with Existing Literature

Topology	Ref.	No. of Control Parameters	Current Stress (A)		Losses (W)		Losses (W)		Efficiency (%)	
					At 200 W		At 500 W			
			200 W	500 W	Cond. Losses	Sw. Losses	Cond. Losses	Sw. Losses	200 W	500 W
DAB with single phase shift control	[30]	1	28.5	31.2	31.19	21.7	36.015	21.11	79.08	89.75
DAB with extended phase shift control	[31]	2	23.42	26.9	19.834	17.631	24.55	18.56	84.24	92.06
DAB with dual phase shift control	[32]	2	23	27.6	14.89	16.66	23.8	18.62	86.37	92.2
DAB with triple phase shift control	[33]	3	23	27.2	17.5	17.75	23.9	18.01	85.01	92.26
Transistor clamped DAB	[34]	3	13.45	18.9	8.41	14.07	17.64	18.65	89.89	93.23
Proposed	Prop.	1	10.2	16.5	7.56	7.81	11.65	8.20	92.86	96.18
Cond.: Conduction losses Sw : Switching losses										

2.6.2 Performance Benefits of Metal Film Capacitor over Electrolytic Capacitor

The selection of type of capacitor significantly effects the reliability of the converter, which is of prime importance in automotive applications. Metal film capacitors are advantageous over electrolytic capacitor when compared in terms of having longer lifespan, however analysis of other performance parameters also play a deciding role in selecting the best suited capacitor. When the ripple current handling capability is considered, the cost of Metal Film poly-propylene-Capacitors ($/A) is about 1/3 of that of Al-Caps. This presents an opportunity of achieving a lower cost and higher power density dc-link design with metal-film in high ripple current applications, like the case in electric vehicles. Due to the formation of resonant tank in the proposed topology, the capacitance value could be reduced and the electrolytic capacitor could be replaced with the metal film capacitor which resulted in reduction in the size of capacitor (capacitance value and physical dimension), reduction in cost and better reliability of the converter.

Further, film capacitors would cost more per microfarad than the electrolytic. Therefore, the advantages of electrolytic capacitor is expected to be more pronounced with high-valued capacitance. But with high voltage application as in electric vehicle, there is another factor of cost that comes into picture. The maximum voltage handling capability of commercially available electrolytic capacitor in market for electrolytic capacitor is only up to 650 V. Applications with bus voltage exceeding 650 VDC need a series parallel combination of aluminum capacitors to handle the voltage and ripple current requirements. Further, balancing resistors are an additional necessity to share the voltage equally across capacitors in series. Whereas, standard DC link Film capacitors are available up to 1500 Vdc. Which means that an assembly of electrolytic capacitor needs to be arranged that counters the expense of metal film capacitor.

Another important aspect of capacitor selection is the equivalent series resistance (ESR) of the capacitor. Aluminum electrolytics have about 10x-15x the ESR of Film capacitors. Film capacitors have lower internal power loss for the same amount of ripple current. Some applications also use large banks of aluminum capacitors just to handle the ripple current. Film capacitors are most economical where high ripple and low capacitance is needed. In addition to the cost, it is to be noted that electrolytic capacitors suffer due to relatively high ESRs, low ripple current ratings, and wear out issue due to evaporation of electrolyte. Metal film capacitors on the other hand provides a well-balanced performance for high voltage applications (e.g., above 500 V) in terms of cost and ESR, capacitance, ripple current and reliability.

Table 2.6 Comparison of Metal Film capacitor with Aluminum electrolytic capacitor

	Metal Film Capacitor B32671P6683K000	**Aluminum electrolytic ALF70C221DF630**
Capacitance value	0.068 µF	220 µF
Voltage Rating	630 V	630 V
Ripple current (A) at 10 kHz 85°C	-	4.58 A
Maximum operating temperature (°C)	125	85
ESR (mΩ)		595
Lifetime (hours)	2,00,000 h at 0.5 * rated voltage, 85 °C	24,000 h at rated voltage and Ripple Current at +85°C
Failure rate	≤ 24 * 10–9/h at 0.5 * V_R, 40 °C	-
End of Life Requirement	-	$40 < V_R \leq 160\ V_{DC}$ Δ C/C < ±20% ESR < 3X ESR Limit, I_L < initial specified limit
Shelf Life	-	2,000 hours at +85°C or 30,000 hours at +40°C 0 VDC
Packaging	radial	radial
Dimension (D, L in mm)	4.0 × 9.0 × 13.0 (w * h * l)	35, 50 mm (Diameter X height)
Volume (mm^3)	468	962.11
Approximate weight (gm)	28.3	80
Cost (per unit in rupees)	₹23.04	₹690

Cost (per unit in $)	$0.283	$8.48

Reliability Test

Test conditions (operating temp/ test voltage/ test hours)	85 °C/ VR,1000 KHz/ 1000 hours	+85°C/ VR/2,000 hours,
Result	No visible damage $\Delta \tan \delta \leq 0.004$	-
Capacitance	$\Delta C/C_0 \leq 5\%$	Within 10% of the initial value
Equivalent Series Resistance		Does not exceed 150% of the initial value
Leakage Current		Does not exceed leakage current limit
Insulation Resistance	Rins ≥ 50% of initial limit	

* The most suited capacitor based on electrical parameters is calculated then the best available choice on Mouser Electronics based on the lowest cost product available is presented.

Based on the above exhaustive analysis, it may be concluded that the cost of metal film capacitor that is required in this application is much less compared to an electrolytic capacitor. Further, the film capacitor is the best choice in terms of cost, performance and reliability for the targeted application in the proposed converter.

2.7 Conclusion

To address the challenges with the resonant dual active bridge converter in application relating to CC-CV charging of Li-ion batteries of electric vehicle, a current driven bi-frequency resonant dual active bridge converter is proposed in this chapter. Its operation at two different but fixed frequencies to behave as a current source and a voltage source makes it a suitable choice of converter for optimal battery charging. The converter behavior is verified through simulation and experimental results. The trajectories of the converter in each interval of operation are derived using state plane analysis and the load characteristics of the presented converter on normalized plane is plotted. It verifies the concept of dual source behavior of the converter to charge a battery in CC and CV mode. The utilization of dual source property of the proposed converter to implement optimal charging strategy directly slashes the control requirement. Thus, the complexity in implementation of charging strategy, the memory requirement, associated cost and the delay is eliminated along with improvement in the converter reliability. A 500 W laboratory prototype of the converter is developed and tested at the resonant frequency and half of the resonant frequency. The experimental results validate the current source and voltage source property of converter and its dynamic performance establishes the robustness of proposed charger during mode transition. Thus, the proposed converter can be suitably used for EV battery charging.

Although, the current driven resonant DAB converter ensures optimal battery charging, it cannot be directly used for very high-power application such as ultra-fast charging. UFC refers to charging a battery quickly, i.e., in few minutes. However, such high-power charging demands hundreds of amperes of current to flow through the converter, producing conduction losses of the order of few kW. Handling such high current and voltage stress across switching devices require exclusive switches that becomes extremely costly and brings device level operational and availability challenges. Further, the heat sink required to dissipate this generated heat attributes impractically large size to the converter making it an unfavorable choice. To address the challenges of UFC application, a current driven fractional power processor is proposed in the next chapter.